Topology optimization of 3D self-supporting structures for additive manufacturing

Langelaar, Matthijs

DOI
10.1016/j.addma.2016.06.010

Publication date
2016

Document Version
Accepted author manuscript

Published in
Additive Manufacturing

Topology Optimization of 3D Self-Supporting Structures for Additive Manufacturing

Matthijs Langelaar

Delft University of Technology, Mekelweg 2, 2628CD Delft, the Netherlands

Abstract

The potential of topology optimization to amplify the benefits of additive manufacturing (AM), by fully exploiting the vast design space that AM allows, is widely recognized. However, existing topology optimization approaches do not consider AM-specific limitations during the design process, resulting in designs that are not self-supporting. This leads to additional effort and costs in post-processing and use of sacrificial support structures. To overcome this difficulty, this paper presents a topology optimization formulation that includes a simplified AM fabrication model implemented as a layerwise filtering procedure. Unprintable geometries are effectively excluded from the design space, resulting in fully self-supporting optimized designs. The procedure is demonstrated on numerical examples involving compliance minimization, eigenfrequency maximization and compliant mechanism design. Despite the applied restrictions, in suitable orientations fully printable AM-restrained designs matched the performance of reference designs obtained by conventional topology optimization.

Keywords: Topology optimization, additive manufacturing, overhang angle, self-supporting designs, manufacturing restrictions

1. Introduction

The field of additive manufacturing (AM) technology is advancing rapidly, with processes becoming more versatile, stable, accurate and economical at a

Email address: m.langelaar@tudelft.nl (Matthijs Langelaar)

steady pace [1, 2, 3]. Key advantages of AM compared to traditional manufacturing techniques are the enormous geometrical freedom it offers to designers, combined with the fact that costs are nearly insensitive to geometrical complexity [4]. This offers opportunities to create highly optimized components where form follows functionality, without the restrictions imposed by conventional manufacturing processes. Capable design optimization tools therefore play an important role in realizing the benefits offered by the AM design freedom [5].

In this context, topology optimization (TO) has been universally recognized as a crucial design technology for AM. TO techniques can generate distributions of material that optimize certain performance criteria defined by the designer, even when an initial design concept is lacking. After its conception in the late 80's [6], TO has developed at a rapid pace and continues to form an area of active research. In various branches of industry, TO is an established part of the design process [7, 8]. For an overview of the field, the reader is referred to recent reviews by Sigmund and Maute [9] and Deaton and Grandhi [10].

While linking TO and AM has the potential to bring significant synergy benefits, an important aspect is currently still missing. Present TO approaches are not tailored to the particular characteristics of AM processes [11]. A limitation encountered in many industrially relevant processes, *e.g.* SLM or EBM, is that the inclination of a downward facing surface (overhang) should remain above a critical value with respect to the baseplate. If this criterion is met everywhere for a given part orientation, the part is said to be self-supporting in that orientation. This common AM limitation has been extensively characterized for various processes [12, 13, 14], and the critical angle is typically found to be in the order of 45°. If a part in its intended build direction contains regions with overhang angles below this critical value, it is not self-supporting and not printable as-is. Consequently, either its geometry must be adjusted, or sacrificial support structures must be included during the build process, and removed afterwards by conventional machining. Both options have clear disadvantages: modifying an optimized geometry inevitably will reduce its performance and

may even render it infeasible, while printing and subsequent removal of support structures increases material, printing and post-processing costs. Efforts have been made to automate and/or optimize the addition of these support structures [15, 16, 17], or to find the most economical sacrificial lattice structures, *e.g.* [18]. Still, instead of minimizing the symptoms caused by an unprintable design, a more desirable option is to address the actual cause.

Because present TO approaches do not account for overhang angle limitations, optimized designs are generally not self-supporting and therefore not printable without applying the outlined, undesirable, measures. Other authors have also recognized this deficiency, and have proposed various potential solutions. Brackett *et al.* (2011) have introduced a method to identify the angle of overhanging sections in 2D designs generated by TO [19], and suggest that this information can be included in the optimization process as an additional constraint. However, no follow-up work has been presented where this has been realized. As an alternative approach, Leary *et al.* (2014) proposed to augment the original optimized design with additional structures [20], such that the final geometry is fully self-supporting. An iterative procedure was developed to limit the amount of added material. In this case, the additional structures are not considered sacrificial parts that must be removed after printing, instead they are part of the final structure. While this approach is successful in generating (2D) self-supporting designs, the final part in general deviates from the original optimized geometry. Recently, Gaynor and Guest (2014) have proposed a wedge-shaped spatial filter to control the boundary orientation of the design during TO [21]. However, the way the filter has been defined does not take into account the layerwise support conditions that must be considered in AM processes, which allows the optimization process to exploit configurations that are not properly self-supporting. When the density average in the wedge exceeded a set threshold, the part above was considered to be properly supported. The published 2D results show that generated designs are indeed self-supporting to a degree, but by only introducing support requirements in an average sense, intermediate density material can readily be used by the optimizer to support fully

dense structures, which is undesirable. In summary, none of the reported approaches successfully achieved optimization of fully self-supporting structures, and in addition the existing work has focused on 2D problems only.

This paper presents a TO approach, compatible with the dominant density-based formulation, that overcomes the problem of unprintable designs and the associated inefficiencies. By including a simplified AM process model in the problem formulation, the overhang angle restriction that applies to the targeted AM processes is rigorously enforced at every step of the optimization process. This is achieved by means of a layerwise applied spatial filter, simulating the printing of the part. The optimization is guided by the performance of the resulting *as-printed* geometry, which leads to self-supporting, fully printable designs. In a preceding study, a 2D version of this AM filter was introduced and investigated [22]. This paper extends its formulation to the 3D case, and demonstrates its performance on a variety of commonly used 3D TO problems, for various build directions. The set of problems considered involves compliance minimization, eigenfrequency maximization and compliant mechanism design.

The paper is organized as follows: Section 2 introduces the concept behind the proposed AM filter approach, and provides its mathematical formulation. Sensitivity analysis is also discussed. Next, Section 3 defines the various test problems for which the effectiveness of the AM filter has been studied. Section 4 discusses the numerical results and actual designs obtained for all test problems, followed by discussion and concluding remarks, in Section 5 and Section 6, respectively.

2. Formulation

2.1. AM filter concept and formulation

To take overhang limitations of AM processes into account during topology optimization, a layerwise filter operation is proposed that transforms a certain *blueprint* design layout into the printable geometry. In this way, the filter acts as a simplified process simulation. This AM filter is defined on a uniform regu-

lar mesh, as is typically used in topology optimization in an early design stage. As a consequence, the resolution of the AM process simulation matches that of the topology optimization design description. The actual AM resolution is usually higher, but regarding the overhang restriction, the design resolution is the limiting factor. For simplicity we consider a cuboid design domain discretized by $n_x \times n_y \times n_z$ cube-shaped finite elements, where the z-direction is the printing direction. To specify a material distribution representing the design, every element in the mesh is associated with a blueprint density variable $b_{(i,j,k)}$. The indices indicate the position of each element, with the first layer on the baseplate having z-index $k = 1$. Our aim is to express the *printed* densities $p_{(i,j,k)}$ in terms of the blueprint densities.

Only elements sufficiently supported by printed elements in the underlying layer can be printed. By definition, all elements supported by the baseplate ($k = 1$) can be printed. In subsequent layers, each element is associated with a supporting region $S_{(i,j,k)}$, consisting of the element directly below the considered element, and the 4 direct neighbors thereof, see Fig. 1. This choice is motivated by the fact that the critical self-supporting overhang angle for the considered processes typically amounts to 45° [12, 13, 14]. In this simplified AM process model, we define that each printed density $p_{(i,j,k)}$ cannot be higher than the maximum printed density in its supporting region, $\hat{p}_S$:

$$p_{(i,j,k)} = \min\left(b_{(i,j,k)}, \hat{p}_S\right) \quad \text{with } \hat{p}_S = \max\left(p \in \ S_{(i,j,k)}\right). \tag{1}$$

At domain boundaries, supporting regions contain fewer than 5 elements, but this is disregarded in the discussion for clarity. By sweeping through the domain from layer 1 to n_z, the printed density field can be constructed.

The operation defined in Eq. 1 is not continuously differentiable due to the nonsmooth min and max operators. As the availability of gradient information is essential for efficient topology optimization, a differentiable version of Eq. 1

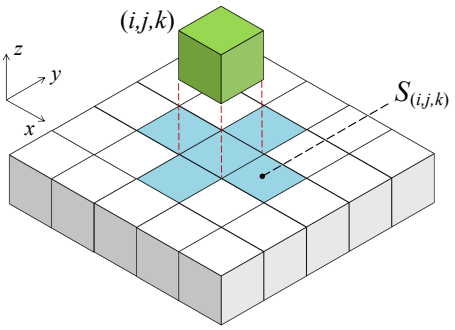

Figure 1: Definition of 3D AM filter. The blue region $S_{(i,j,k)}$ denotes the supporting region of an element at position (i, j, k) in a mesh. When insufficient printed material is present in this region, the green element (i, j, k) cannot be printed.

is proposed that employs the following smooth approximations:

$$\min(b, \hat{p}_S) \approx \text{smin}(b, \hat{p}_S) = \frac{1}{2}\left(b + \hat{p}_S - \left((b-\hat{p}_S)^2 + \varepsilon\right)^{1/2} + \sqrt{\varepsilon}\right), \quad (2)$$

$$\max\left(p \in \ S\right) \approx \text{smax}(p \in \ S) = \tilde{p}_S = \left(\sum_{e \in \ S} p_e^P\right)^{1/Q}. \quad (3)$$

Note that other smooth approximation choices are possible, yet these were found to yield the desired behavior [22] and have been used in this paper in all numerical examples. The parameters ε, P and Q control the smoothness and accuracy of these approximations. Smaller ε and larger P and Q values reduce approximation errors, but increase nonlinearity. In this paper the following default values are applied:

$$\varepsilon = 10^{-4}, \quad P = 40, \quad Q = P + \log(5)/\log(p_0), \quad p_0 = 0.5. \quad (4)$$

The parameter p_0 indicates the density value for which the smooth max operator gives exact results for layers of uniform printed density, as can be verified by substitution in Eq. 3. For $p_0 \to 0$, $Q \to P$ and the conventional P-norm is retrieved, while choosing $0 < p_0 \leq 1$ introduces a slight penalization of the P-norm approximation. This prevents overestimation of the support capacity of densities below p_0, which effectively suppresses the formation of 'porous' support

structures. Numerical tests indicate that using $p_0 = 0.5$ gives superior topology optimization results compared to the unaltered P-norm. For a more detailed study and discussion of the effect these parameters, we refer to [22].

2.2. Sensitivity analysis

After applying the AM filter, the printed density field $\mathbf{p}$ is obtained. The performance of this printed design is evaluated using *e.g.* finite element analysis. For gradient-based optimization, sensitivities of each response f with respect the blueprint variables $\mathbf{b}$ are required. Given sensitivities $\partial f/\partial \mathbf{p}$ obtained by (adjoint) sensitivity analysis, the transformed sensitivities $\partial f/\partial \mathbf{b}$ are given by:

$$\frac{\partial f}{\partial \mathbf{b}_k} = \boldsymbol{\lambda}_k^T \frac{\partial \mathrm{smin}}{\partial \mathbf{b}_k}, \tag{5}$$

$$\boldsymbol{\lambda}_k^T = \frac{\partial f}{\partial \mathbf{p}_k} + \boldsymbol{\lambda}_{k+1}^T \frac{\partial \mathrm{smin}}{\partial \mathbf{p}_k} \qquad \text{for } 1 < k < n_z, \qquad \boldsymbol{\lambda}_{n_z}^T = \frac{\partial f}{\partial \mathbf{p}_{n_z}}. \tag{6}$$

Here subscripts are layer indices, and $\boldsymbol{\lambda}_k$ denote layerwise multiplier fields introduced for the purpose of adjoint sensitivity analysis. The full derivation of these expressions is given in the Appendix. Given the mutual dependencies as described by Eq. 6, the multipliers can be evaluated by sweeping through the domain in reverse printing direction, from the top layer to the base layer. Sensitivities $\partial f/\partial \mathbf{b}$ subsequently follow from Eq. 5. [22] The base layer ($k = 1$) is treated separately: since by definition $\mathbf{p}_1 = \mathbf{b}_1$, we find $\partial f/\partial \mathbf{b}_1 = \partial f/\partial \mathbf{p}_1$. The derivative $\partial \mathrm{smin}/\partial \mathbf{p}$ in Eq. 6 follows from differentiation of Eqs. 1, 2 and 3:

$$\begin{aligned}
\frac{\partial \mathrm{smin}}{\partial \mathbf{p}} &= \frac{\partial \mathrm{smin}(b, \tilde{p}_S)}{\partial \tilde{p}_S} \frac{\partial \tilde{p}_S}{\partial \mathbf{p}}, \text{ with} \\
\frac{\partial \mathrm{smin}(b, \tilde{p}_S)}{\partial \tilde{p}_S} &= \frac{1}{2}\left(1 + (b - \tilde{p}_S)\left((b - \tilde{p}_S)^2 + \epsilon\right)^{-1/2}\right), \text{ and} \\
\frac{\partial \tilde{p}_S}{\partial p_i} &= p_i^{P-1} \frac{P}{Q} \left(\sum_{e \in S} p_e^P\right)^{1/Q-1}.
\end{aligned} \tag{7}$$

In the last expression, only printed densities p_i that are located in the support region of the considered element give a contribution. Both sensitivity analysis and application of the AM filter itself do not involve intensive computations: in

the 3D problems considered in this study, the total computational cost related to the AM filter formed less than 1% of the cost of the entire optimization.

3. Test problems

The next subsections describe the test problems used to investigate and illustrate the performance of the proposed AM filter. They involve three standard problem types, typically encountered in practical applications of topology optimization. The results of these tests are presented in Section 4. Our interest is in aspects related to the AM filter performance, rather than the particular numerical outcome of these specific test cases. Nevertheless, complete problem descriptions are provided for completeness.

In all cases, linear elastic isotropic material is used with a Young's modulus of 211 GPa, Poisson ratio of 0.33, material density 7850 kg/m^3. Furthermore, the conventional density-based topology optimization approach using SIMP material interpolation [23] is applied, with a penalization exponent of 3.0. To control minimum feature size and prevent checkerboarding, consistent density filtering [24] is used to generate the blueprint design field $\mathbf{b}$ from base design variables associated to each element, with the applied radius indicated at each case. The main sensitivity expressions are given for completeness, derivations can be found in literature for these conventional problems, *e.g.* [25]. Classical isoparametric, cubic 8-node finite elements with trilinear shape functions are used. Unless specified otherwise, the optimization process is initialized with a uniform distribution of the available material.

3.1. Compliance minimization

Minimization of compliance is an important and frequently considered topology optimization problem. In the present AM filter setting it is formulated

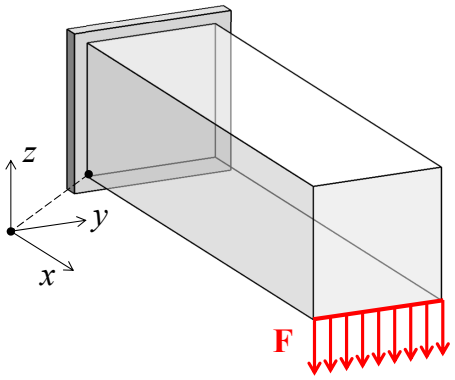

Figure 2: Beam problem used in numerical compliance minimization tests.

as:

$$\begin{aligned} \min_{\mathbf{b}} \quad & C = \mathbf{f}^T \mathbf{U}(\mathbf{p}) \\ \text{s.t.} \quad & V(\mathbf{p})/V_{\max} - 1 \leq 0, \\ & \mathbf{K}(\mathbf{p})\mathbf{u}(\mathbf{p}) = \mathbf{f}, \\ & 0 \leq \mathbf{b} \leq 1. \end{aligned} \tag{8}$$

Here $\mathbf{K}$, $\mathbf{u}$ and $\mathbf{f}$ denote the finite element system stiffness matrix, displacement vector and load vector, respectively, and V and $V_{\max}$ are the actual and allowed volume of the printed part. Note that compliance C and volume V are evaluated on the printed density field $\mathbf{p}$, while the optimization process controls the blueprint field $\mathbf{b}$. The transformation of these fields and the associated design sensitivity information is governed by the procedures formulated in Section 2. The sensitivity of the objective with respect to the printed density field $\mathbf{p}$ is given by:

$$\frac{\partial C}{\partial p_i} = -\mathbf{u}^T \frac{\partial \mathbf{K}}{\partial p_i} \mathbf{u}. \tag{9}$$

The considered test problem consists of a cuboid domain meshed with 150×50×50 elements shown in Fig. 2, with a 100 N total load distributed over the lower front edge. All displacements at the back face of the domain ($x = 0$ plane) are

suppressed. $V_{\max}$ is chosen as 30% of the domain volume, and the filter radius is set to 1.5 times the element edge length.

3.2. Eigenfrequency maximization

When the dynamic performance of a component is of interest, an eigenfrequency maximization can be performed. As a test problem we consider a simplified motion platform, used *e.g.* in high-speed positioning tasks in mechatronic systems. The design domain, meshed by $120\times160\times40$ elements, is depicted in Fig. 3. The top layer of the domain is a solid non-design region. The remaining volume can be occupied up to 25% by the rest of the design. As an additional constraint, the second eigenfrequency should be kept a certain factor above the first. This problem can be stated as:

$$\begin{aligned} \min_{\mathbf{b}} \quad & 1/\omega_1^2(\mathbf{p}) \\ \text{s.t.} \quad & V(\mathbf{p})/V_{\max} - 1 \leq 0, \\ & 1.1 - \omega_2^2(\mathbf{p})/\omega_1^2(\mathbf{p}) \leq 0, \\ & \left(\mathbf{K}(\mathbf{p}) - \omega_i^2(\mathbf{p})\mathbf{M}(\mathbf{p})\right)\mathbf{v}_i(\mathbf{p}) = 0, \qquad i = 1,2 \\ & 0 \leq \mathbf{b} \leq 1. \end{aligned} \tag{10}$$

Here $\mathbf{M}$ denotes the mass matrix, $\mathbf{v}_i$ and ω_i are the i^{th} eigenvector and angular eigenfrequency. The lowest two structural free vibration modes are considered, rigid body modes are removed using deflation. The sensitivity of a squared eigenfrequency ω_i^2 with respect to $\mathbf{p}$ is given by:

$$\frac{\partial \omega_i^2}{\partial p_j} = \mathbf{v}_i^T \left(\frac{\partial \mathbf{K}}{\partial p_j} - \omega_i^2 \frac{\partial \mathbf{M}}{\partial p_j} \right) \mathbf{v}_i \Big/ \left(\mathbf{v}_i^T \mathbf{M} \mathbf{v}_i \right). \tag{11}$$

For this problem, the initial design is a fully solid design domain. In our experience, this initial configuration often leads to better results in eigenfrequency problems, compared to starting with the allowed volume fraction. Furthermore, to suppress irrelevant low-frequency modes in void regions, in addition to stiffness penalization also mass penalization with exponent 5.0 is applied for elements with density values below 0.1. The filter radius was set to 2.0 times the element edge length.

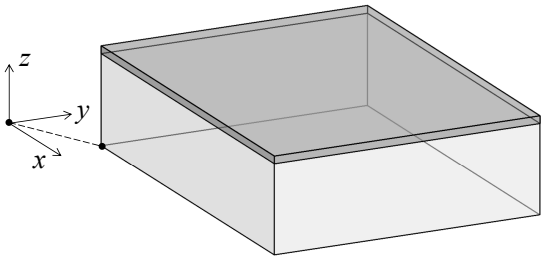

Figure 3: Design domain used in the eigenfrequency maximization of a motion platform. The dark gray region consists of solid non-design elements.

3.3. Compliant mechanism

The third problem type is a compliant gripper, as depicted in Fig. 4. The domain consists of $160 \times 60 \times 140$ elements, and the filter radius is 3.0 times the element edge length. Distributed input loads are applied to the green boxes, and the gripper output to be maximized is defined by the closing motion in z-direction of the blue jaws. Between the jaws, a void non-design region is defined. To all nodes of the jaws, a workpiece stiffness is applied using springs acting in z-direction with a of stiffness 5 kN/m. We impose symmetry with respect to the domain midplanes in y- and z-direction and analyze only the upper left quarter of the domain. In terms of element units, the various boxes span the following ranges in this $160 \times 30 \times 70$ quarter of the domain: input region [1-40, 24-30, 54-56], jaw region [136-160, 25-30, 11-12], and void region [136-160, 1-30, 1-10].

Three loadcases are considered in this problem: the first concerns the operation of the gripper, with load $\mathbf{f}_1 = 1$ kN applied to the input region and jaws unblocked. The other cases serve to control the overall stiffness of the mechanism. In the second loadcase, no input force is applied and the displacement of the input regions is suppressed. Simultaneously, a distributed load $\mathbf{f}_2$ with resultant (0, 1500, 500) N is applied to the jaw. In the third case, the jaw motion is blocked while applying the input load $\mathbf{f}_3 = \mathbf{f}_1$ to the input region.

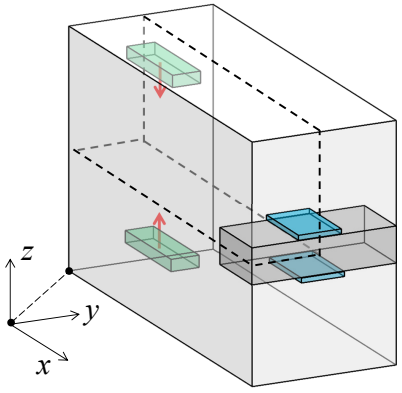

Figure 4: Design domain and input/output regions used in the optimization of a compliant gripper. The dark gray region represents a void non-design region. Due to symmetry, only a quarter of the domain is considered in the optimization, indicated by dashed lines.

The optimization problem for this compliant gripper is defined as:

$$\begin{aligned} \min_{\mathbf{b}} \quad & f = \mathbf{l}_{out}^T \mathbf{u}_1(\mathbf{p}) \\ \text{s.t.} \quad & V(\mathbf{p})/V_{\max} - 1 \leq 0, \\ & \mathbf{K}_i(\mathbf{p})\mathbf{u}_i(\mathbf{p}) = \mathbf{f}_i \qquad \text{with} \quad i = 1,2,3, \\ & \mathbf{f}_i^T \mathbf{u}_i(\mathbf{p})/C_i - 1 \leq 0 \qquad \text{with} \quad i = 2,3, \\ & 0 \leq \mathbf{b} \leq 1. \end{aligned} \tag{12}$$

Here $\mathbf{l}_{out}$ is a sparse vector containing unity values at z-degrees of freedom in the jaw region, such that the inner product $\mathbf{l}_{out}^T \mathbf{u}_1$ results in a measure of the desired motion. Maximum compliances C_2, C_3 in loadcase 2 and 3 are chosen as 20 Nmm and 100 Nmm, respectively. The maximum volume $V_{\max}$ is set to 20% of the design domain. The sensitivity of the objective with respect to the part design field $\mathbf{p}$ is given by:

$$\frac{\partial f}{\partial p_i} = -\mathbf{a}^T \frac{\partial \mathbf{K}}{\partial p_i}\mathbf{u} \quad \text{with} \quad \mathbf{K}\mathbf{a} = \mathbf{l}_{out}. \tag{13}$$

Compliance sensitivities are analogous to Eq. 9.

4. Results

The following subsections present the results of various numerical test problems. In all optimizations, the gradient-based optimization algorithm Method of Moving Asymptotes [26] was used, and sufficient iterations were performed to at least converge to a relative change in objective values between subsequent iterations below 0.1%. Subsequently, the designs described by 3D density fields have been post-processed for visualization by isosurface extraction at a density value of 0.3, resulting in a triangulated surface mesh. To quantify the printability of the obtained designs in various orientations, two criteria are considered:

1. Printable volume fraction. By applying the AM filter to the final design in a particular printing orientation, followed by isosurface extraction and volume computation, the printable volume fraction with respect to a reference design is computed. NetFabb software was used to evaluate the volume of the extracted STL geometry.
2. Infeasible overhanging surface fraction. This is determined by computing the overhang angle of every individual triangular facet of the extracted isosurface, using its normal and the considered printing orientation. In this paper, we define the overhang angle as the angle between baseplate and part surface, and consider 45° as the critical angle, with shallower angles being infeasible. Infeasible overhanging facets can be identified, and their fraction weighted by total facet surface area is reported.

The first quantity indicates which fraction of a design is self-supporting, the second gives a (rough) indication of the amount of additional support material that a design would require.

Adequately depicting three-dimensional results in a 2D medium poses a challenge. The discussion of the various cases highlights several particular aspects, but for a complete impression of the designs, the full 3D geometries are provided in U3D format as digital supplements to this article, as well as embedded in the digital document.

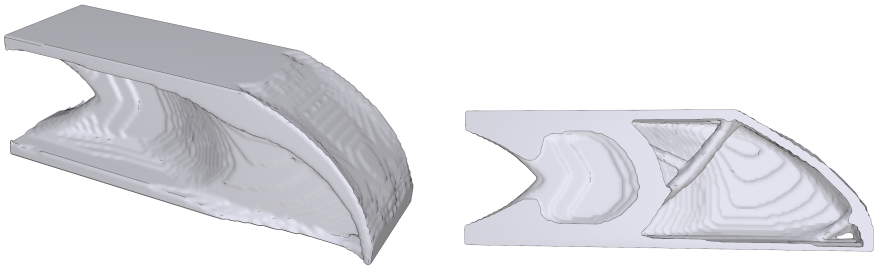

Figure 5: Beam design obtained for the reference case, without AM filter applied. The cut-away view reveals its internal structure.

4.1. Compliance minimization

Fig. 5 shows the beam design obtained when no AM filter is applied. This serves as the reference design to compare relative performance. When evaluating, for example, the printability of this design using the plane $z = z_{\min}$ as the baseplate (in short: $z_{\min}$ baseplate), it can be seen in Fig. 6 that a significant fraction of the overhanging surfaces exceeds the critical angle. For this case, 12.2% of the total surface has an infeasible orientation, and this percentage excludes the surface contacting the baseplate.

If this design were to be printed, without the use of additional support material, the resulting part is shown in Fig. 7(a). In this case, only 83% of the full part volume is printable, and important load-bearing sections are removed or weakened. When using topology optimization with the proposed AM-filter, for this printing orientation a modified design is generated, depicted in Fig. 7(b). This design is fully printable without additional supports, *i.e.* its printable volume fraction is 100%. It can be seen that significant changes have occurred in the geometry, where two top beams with V-shaped cross sections replace the I-beam profile present in the reference design. The facet angles with respect to the baseplate of this AM-optimized design are shown in Fig. 8, together with

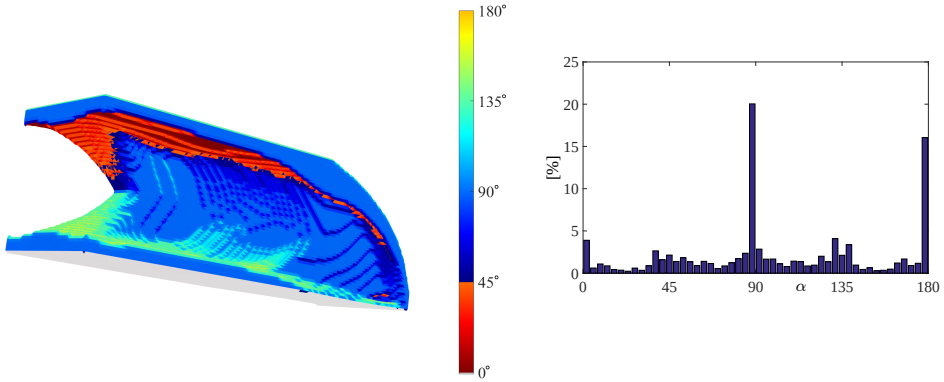

Figure 6: Local facet angles with respect to the $z_{\min}$ baseplate of the reference beam design, and their area-weighted histogram. The surfaces in contact with the baseplate (shown in gray) are excluded.

the angle histogram. It can be seen that the optimization process has avoided any surfaces with angles shallower than 45°, in accordance with the specified critical overhang angle. The 45° orientation shows a bigger peak than most other orientations, indicating that it is advantageous for certain surfaces to be close to the limit. The peaks at 90° and 180° are due to the flat side and top surfaces of the domain.

Beam designs for six baseplate orientations are depicted in Fig. 9. In all cases the default AM filter parameters have been used, except for the case where the baseplate corresponds to the $x_{\min}$ plane, where $p_0 = 0.1$ was used. With the default $p_0 = 0.5$ value, the connection between support and load was lost in the first iterations, which prevented the optimizer from finding a suitable design. It is clear that the optimized designs are affected by the selected printing orientation, and that the optimization process finds different, orientation-specific solutions to circumvent the AM manufacturing constraints imposed by the AM filter. To assess the printability of these designs, the printable volume of each individual design in all six orientations is reported in Table 1. It shows that each design is fully printable without additional supports (100% printable volume) in

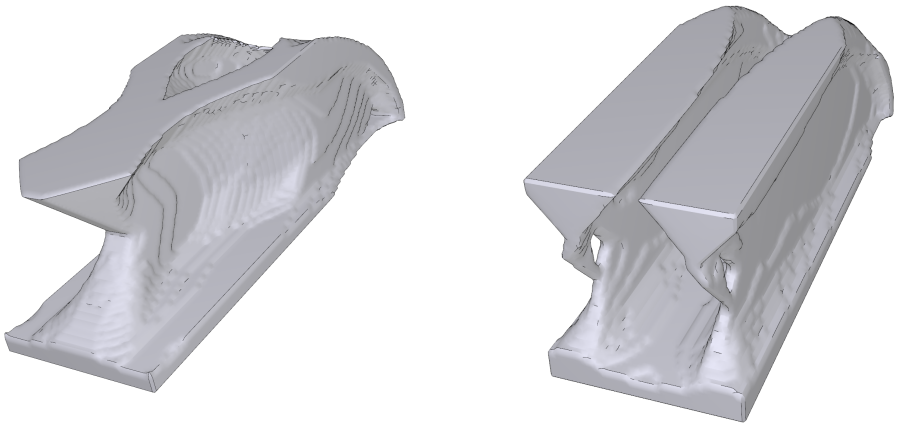

a) Printable part of reference design b) AM-optimized design for $z_{\min}$ baseplate

Figure 7: Reference and AM-optimized beam designs printed from the $z_{\min}$ baseplate.

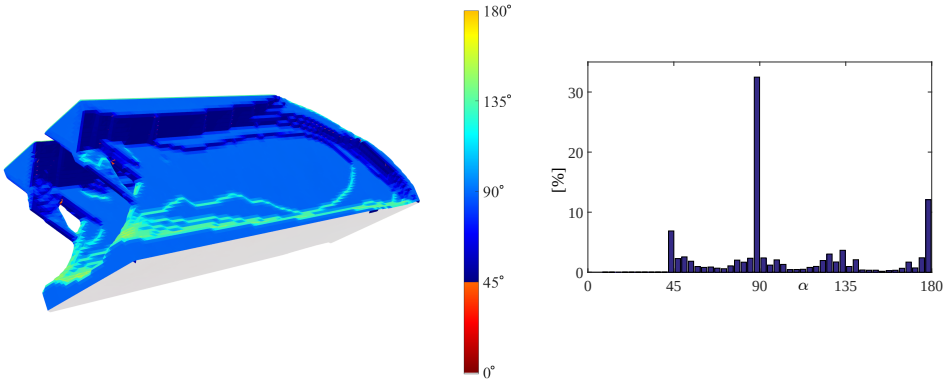

Figure 8: Local facet angles with respect to the $z_{\min}$ baseplate of the $z_{\min}$ AM-optimized beam design, and their area-weighted histogram. The surfaces in contact with the baseplate (shown in gray) are excluded.

Table 1: Printable volume fractions in different printing orientations given by baseplate plane, of beam designs (vertical) obtained for different orientations used in the optimization process. Reference designs are those designed for and printed in corresponding orientations.

Design case	Printing orientation (baseplate)					
	$x_{\min}$	$x_{\max}$	$y_{\min}$	$y_{\max}$	$z_{\min}$	$z_{\max}$
Free	99%	93%	78%	78%	83%	72%
$x_{\min}$	**100**%	97%	74%	74%	82%	69%
$x_{\max}$	100%	**100**%	61%	60%	95%	83%
$y_{\min}$	98%	94%	**100**%	9%	91%	81%
$y_{\max}$	98%	94%	9%	**100**%	91%	82%
$z_{\min}$	80%	95%	55%	55%	**100**%	80%
$z_{\max}$	99%	97%	48%	48%	93%	**100**%

the orientation for which it has been optimized. Also the infeasible overhanging surface fractions listed in Table 2 show minima at orientations corresponding to those used in the optimization. Fractions range from 0.02% to 0.92%, with the highest value seen in the $y_{\min}$ orientation. Note also that the reference design is almost printable in the $x_{\min}$ orientation, with an infeasible surface fraction of only 1.79% and a printable volume fraction of 99%.

In addition, Table 2 lists the relative compliance achieved by the AM-restricted designs, compared to the reference design. This shows that in most orientations, designs reach compliance values near or even slightly superior to (*i.e.* lower than) the reference performance. In all cases, the volume constraint was active. From this, we can conclude that the obtained reference design is a local optimum, as alternative designs (*e.g.* $z_{\min}$, $z_{\max}$) show better performance. Convergence to local optima is practically a certainty in 3D topology optimization, which concerns large-scale non-convex optimization problems [27]. In these z-orientation cases, the AM filter has triggered the optimization process to take a different path through the design space, to arrive at superior local optima compared to the reference case.

Only in the $y_{\min}$ and $y_{\max}$ orientations, a noticeable 7% compliance deterior-

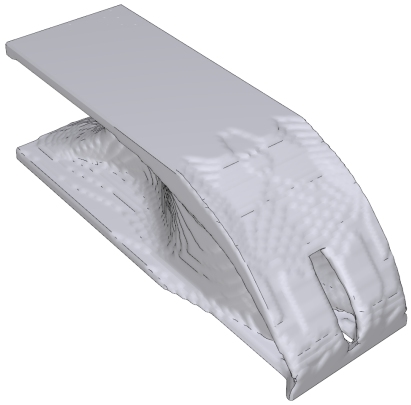

a) Optimized beam for $x_{\min}$ baseplate

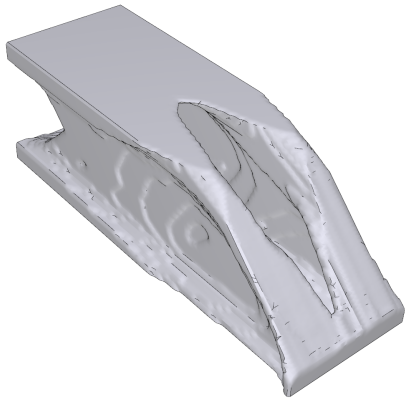

b) Optimized beam for $x_{\max}$ baseplate

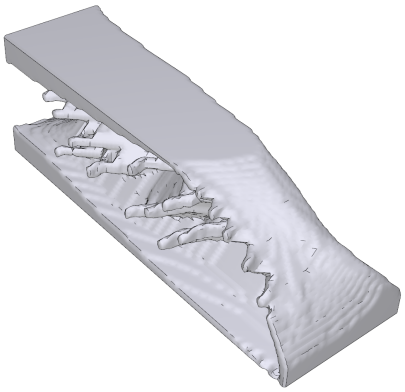

c) Optimized beam for $y_{\min}$ baseplate

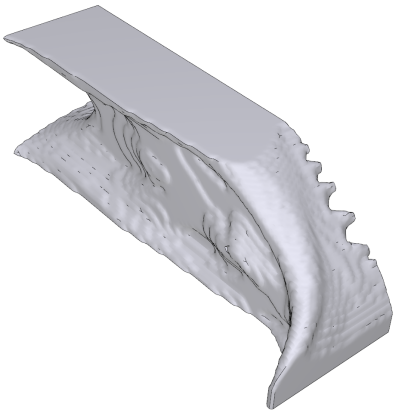

d) Optimized beam for $y_{\max}$ baseplate

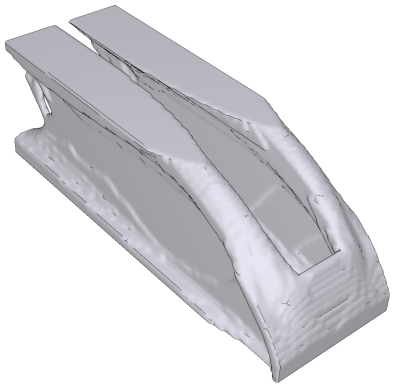

e) Optimized beam for $z_{\min}$ baseplate

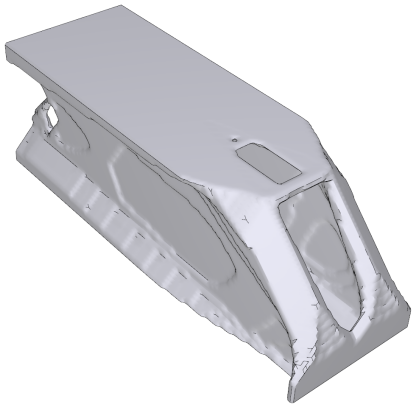

f) Optimized beam for $z_{\max}$ baseplate

Figure 9: AM-optimized beam designs for various orientations.

Table 2: Relative compliance values (lower is better) and infeasible overhanging surface fractions in different printing orientations given by baseplate plane, of beam designs obtained for different orientations used in the optimization process. Bold numbers indicate a printing orientation matching the one used during optimization.

Design case	Compliance (normalized)	Printing orientation (baseplate) $x_{\min}$	$x_{\max}$	$y_{\min}$	$y_{\max}$	$z_{\min}$	$z_{\max}$
Free	100%	1.79%	1.60%	14.7%	14.7%	12.2%	16.2%
$x_{\min}$	101%	**0.21**%	1.84%	15.9%	16.0%	12.4%	15.9%
$x_{\max}$	100%	0.72%	**0.02**%	22.6%	22.0%	6.25%	12.1%
$y_{\min}$	107%	4.46%	4.42%	**0.92**%	17.3%	11.1%	14.4%
$y_{\max}$	107%	3.79%	3.39%	17.6%	**0.79**%	11.2%	14.9%
$z_{\min}$	99%	1.82%	1.86%	24.0%	23.8%	**0.04**%	12.0%
$z_{\max}$	98%	1.13%	0.55%	26.2%	26.2%	8.09%	**0.02**%

ation is observed. The reason for this becomes clear when inspecting the design, *e.g.* Fig. 9(c): strut-like structures have formed, which serve as support structures for the midsection of the beam. These structures have no direct role in improving the compliance of the beam itself, but enable the fabrication of the midsection, which contributes to the objective. So in case it is advantageous for the overall performance, the proposed optimization process is able to generate support structures where necessary.

The higher infeasible overhanging surface fractions observed for $y_{\min}$ and $y_{\max}$ designs are also related to these support structures. This is seen in Fig. 10, which depicts the facet angle distribution for the $y_{\min}$ baseplate case. Red facets indicate shallower angles than the critical 45° overhang angle. These infeasible facets occur predominantly between the connecting points of supporting structures with the midsection of the beam, where transitions from +45° to -45° surfaces take place. By a combination of the isosurface extraction process, the finite mesh resolution, and the density filtering used to impose a length-scale on the problem, such sharp transitions cannot be resolved. This results in more gradual transitions in the extracted 3D geometry, where facets at the cusps ex-

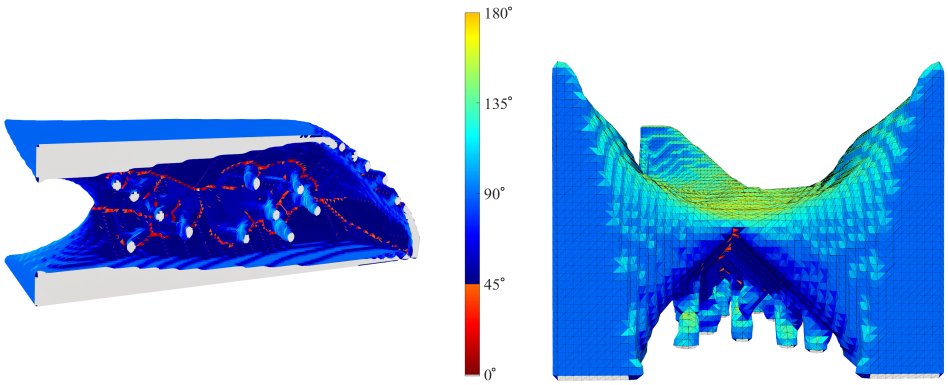

Figure 10: Local facet angles with respect to the $y_{\min}$ baseplate of the $y_{\min}$ AM-optimized beam design. The surfaces in contact with the baseplate (shown in gray) are excluded.

hibit infeasible orientations. This design could be adapted by sharpening these cusps to proper +45°/-45° transitions. Moreover, experiments show that small overhanging sections are in fact still printable [17, 14]. Since the infeasible facets in this design are localized, the part might even be printable without adaptation.

4.2. Platform eigenfrequency maximization

Also for the motion platform a reference design is optimized, as well as a design where the AM filter is applied. We choose to consider only the $z_{\max}$ baseplate case, as this forms the most natural part orientation given the non-design solid plate on top of the domain. Fig. 11 depicts the obtained designs, and Table 3 and Table 4 list the printable volume fraction, infeasible angle surface fraction, and relative performance, respectively. The design with AM restrictions has quite a different geometry and is 15% lighter compared to the reference case, but both designs achieve the same first eigenfrequency.

The printability indicators in Table 3 and Table 4 again confirm that the design optimized with AM-filter is fully printable in the orientation optimized for, similar to the preceding beam cases. The reference design, instead, requires additional support material (which may not be easily removable). Comparing

Table 3: Printable volume fractions in different printing orientations given by baseplate plane, of platform designs (vertical) obtained for different orientations used in the optimization process. Reference designs are those designed for and printed in corresponding orientations.

Design case	Printing orientation (baseplate) $x_{\min}$	$x_{\max}$	$y_{\min}$	$y_{\max}$	$z_{\min}$	$z_{\max}$
Free	71%	71%	87%	87%	58%	82%
$z_{\max}$	94%	94%	84%	84%	39%	**100**%

Table 4: Relative first eigenfrequency values (higher is better) and infeasible overhanging surface fractions in different printing orientations given by baseplate plane, of platform designs obtained for a particular orientation used in the optimization process. Bold numbers indicate a printing orientation matching the one used during optimization.

Design case	Objective (normalized)	Printing orientation (baseplate) $x_{\min}$	$x_{\max}$	$y_{\min}$	$y_{\max}$	$z_{\min}$	$z_{\max}$
Free	100.0%	8.73%	8.72%	5.10%	5.10%	21.0%	9.20%
$z_{\max}$	100.1%	2.42%	2.40%	7.37%	7.37%	30.7%	**0.30**%

the designs shown in Fig. 11, both feature an additional hollow box attached to the given rectangular plate. This additional structure stiffens the plate and thereby increases its eigenfrequency. However, the reference design features a much larger box than the AM-optimized design, with a large, unsupported closing plate parallel to the rectangular non-design plate. The AM-optimized design shows a central strut supporting a much smaller closing plate of the box when printing from the $z_{\max}$ baseplate. The strut extends from the given rectangular plate and ends in a dome-like structure with +45°/-45° surfaces, that shows some similarity to structures seen in the midsection of the beam design optimized for y-oriented printing directions, see Fig. 10(c,d). A difference in this eigenfrequency case is that central strut is likely to contribute to the overall performance, while those in Fig. 10 have no mechanical function but only serve to enable printing of the midsection of the beam.

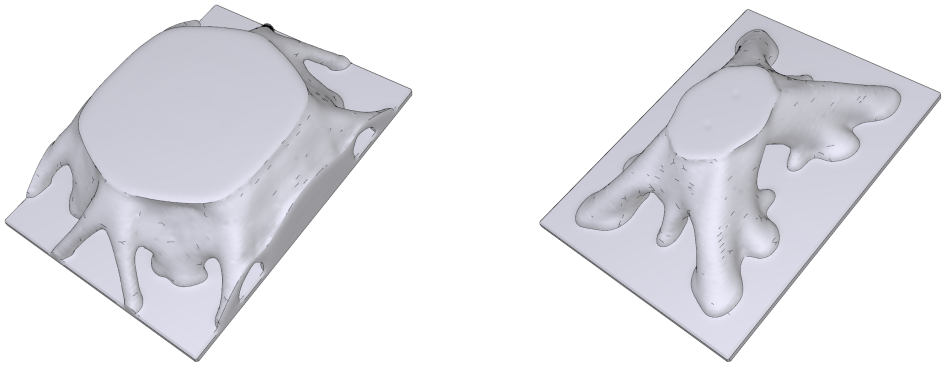

a) Reference design

b) AM-optimized design for $z_{\max}$ baseplate

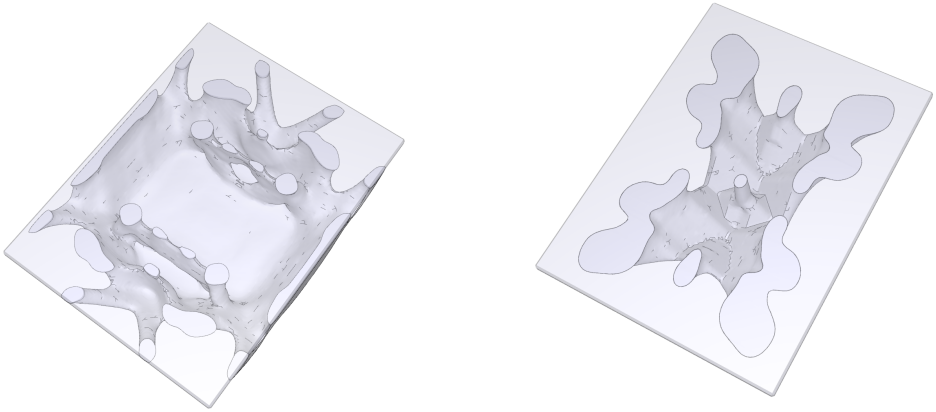

c) Reference case with transparent plate

d) AM-optimized case with transparent plate

Figure 11: Reference and AM-restricted motion platform design optimized for maximum first eigenfrequency. The solid top plate has been made transparent to reveal the internal structures.

Table 5: Relative jaw motion values (higher is better), infeasible overhanging surface fractions and printable volume fractions in relevant printing orientations given by baseplate plane, of gripper designs obtained for different orientations used in the optimization process. Bold numbers indicate a printing orientation matching the one used during optimization.

Design case	Jaw motion (normalized)	Infeasible surface fraction		Printable volume fraction	
		$x_{\min}$	$x_{\max}$	$x_{\min}$	$x_{\max}$
Free	100%	5.70%	6.05%	95%	91%
$x_{\min}$	61%	**0.01**%	4.81%	**100**%	97%
$x_{\max}$	107%	4.70%	**2.30**%	95%	**100**%

4.3. Compliant gripper design

To limit computational costs of the compliant gripper optimization, only a quarter of the full domain was used, implying twofold symmetry. Because of this choice, only the printing directions aligned with the x-axis are relevant. The resulting mechanisms without and with AM restrictions are depicted in Fig. 12. All three designs have similar topologies, but differ in jaw and hinge shapes. Table 5 reports relative performance (jaw motion) and printability indicators. It is seen that the $x_{\min}$ design only reaches 61% of the reference jaw motion, but the $x_{\max}$ design (Fig. 12(c)) exceeds the reference performance by 7%. In terms of printability both designs optimized with the AM-filter show 100% printable volume, but regarding the infeasible facet angle, the well-performing $x_{\max}$ design shows a relatively high 2.3% surface fraction. Upon inspection, it turns out that mainly the slanted surfaces near the jaw area are recognized as infeasible, as shown in Fig. 13. These facets have an inclination slightly below 45°, there are no large deviations from the critical overhang angle as is also seen in the angle histogram in Fig. 13. When relaxing the critical angle to 44.9°, the area fraction of infeasible facets reduces to only 0.21%. The slight deviation from 45° may have been caused by the isosurface extraction post-processing step, but for all practical purposes this does not negatively affect the utility of the obtained gripper design.

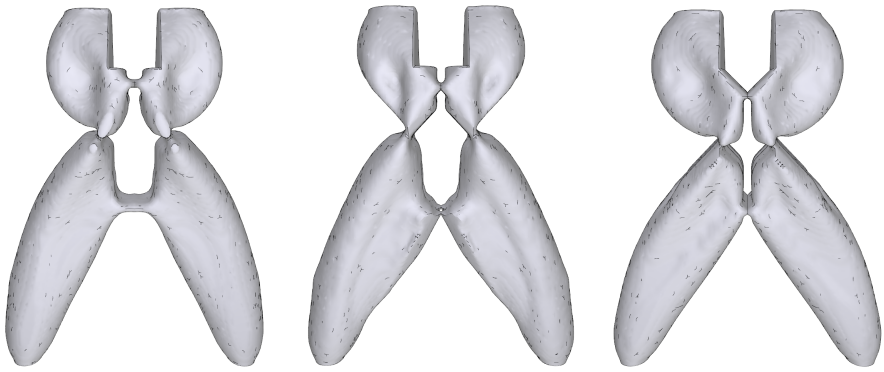

a) Reference design b) $x_{\min}$ baseplate c) $x_{\max}$ baseplate

Figure 12: Reference and AM-restricted compliant gripper designs.

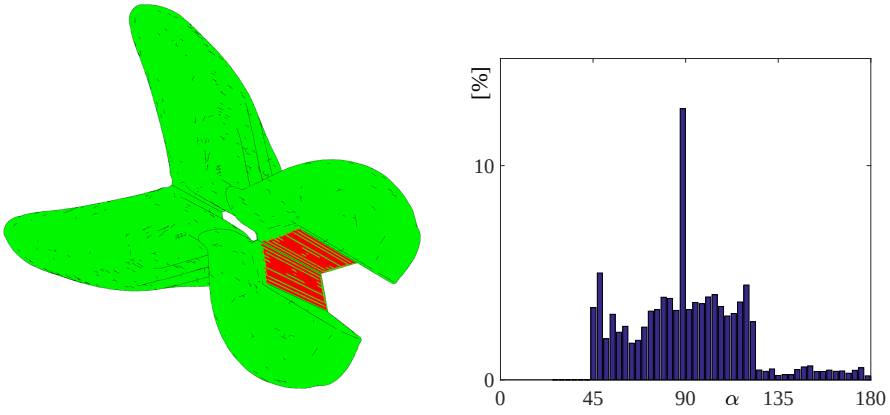

Figure 13: Feasible (green) and infeasible facet angles (red) of the gripper design of the $x_{\min}$ baseplate case, and a histogram of the facet angle distribution. Surfaces in contact with the baseplate are excluded.

4.4. Influence of AM filter on printable designs

In some design cases, topology optimization without AM restrictions produces printable designs. In this section we investigate if the same designs are obtained when the AM filter is applied. To this end, compliance minimization of two short beam problems shown in Fig. 14 is considered. The load is distributed over a square centered region, with an area of 4% of the front face. The design domain in Fig. 14(a) is clamped over its entire back face, while the domain in Fig. 14(b) is only clamped in the corners, by square patches each occupying 4% of the back face area. All other settings are the same as in Section 3.1. The 'free' designs (i.e. obtained without using the AM filter), shown in the center column of Fig. 14, are fully printable for a baseplate in $x_{\max}$ position. When repeating the optimization with AM filter in the corresponding orientation, designs are obtained that are topologically similar, as shown in the right column of Fig. 14. However, the exact geometries of the AM-restricted designs are different from their free counterparts: the middle section in case (a) is thicker, and the separation between the arms in case (b) is larger. Also in terms of performance, slight differences were observed: in case (a), the AM-restricted design showed 0.8% better compliance, while in case (b), the AM-restricted design performed 1.0% worse than the free result.

At first sight, it may seem strange that fully printable designs are not exactly reproduced by the AM-restricted optimization. But while the final result of the free optimization is printable, this does not hold for all intermediate designs in each iteration of the optimization process. As the AM filter extracts the printable part of a design in every iteration, the AM-restricted optimization follows a different path through the design space than the unrestricted case. This is likely to be the main reason behind the different outcomes. Fig. 15, which shows the density distributions early in the optimization process for the free and AM-restricted optimization of the first short cantilever case, clearly illustrates the difference. In the free case (Fig. 15(a)), high-density elements (depicted in blue) can form without being supported by other high-density structures. In contrast, the AM filter prevents this, and forces the optimization process to

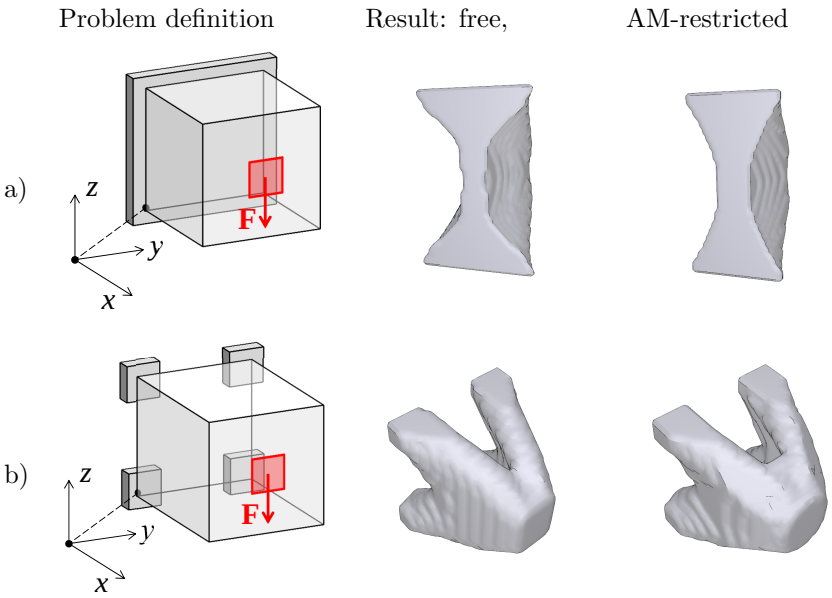

Figure 14: Short beam problems that yield self-supporting designs without AM filter. Case (a) is defined on a 30×50×50 element mesh, case (b) involves a mesh of 30×30×30 elements. In both cases, a 30% volume constraint is used.

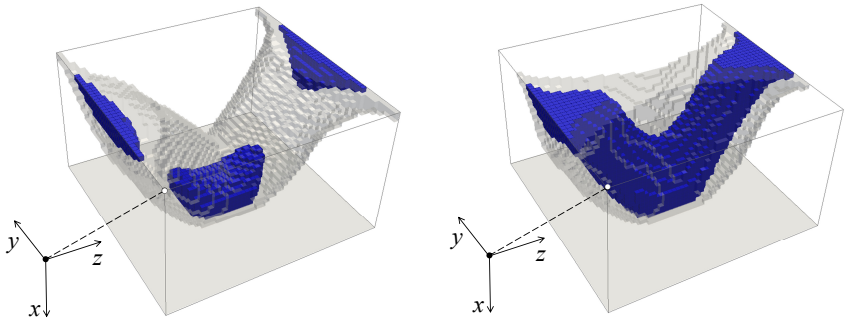

a) Free design b) AM-restricted design

Figure 15: Intermediate design state at an early stage of the optimization process (10^{th} iteration), for the free (left) and AM-restricted case of the short beam problem defined in Fig. 14(a). In this view, the bottom face represents the baseplate. Blue elements have densities of 95% and higher, while the semi-transparent elements have at least 50% density.

create properly supported features, as seen in Fig. 15(b).

If the considered optimization problem was convex and its global optimum printable, still both cases should converge to the same result. However, as topology optimization problems are high-dimensional non-convex optimization problems, many local optima exist. Whether the free or the AM-restricted case ends up with the best-performing design is not predictable, this strongly depends on starting point, optimizer settings, and the particular case considered. However, our numerical experiments indicate that performances typically are very close, and the examples in this paper demonstrate that the AM filter certainly does not restrict the gradient-driven optimization process from converging to a well-performing solution.

5. Discussion

The preceding numerical examples demonstrate that, by including the proposed AM filter in conventional density-based topology optimization procedures, designs can be generated that are fully printable, in the sense that they fulfill geometrical requirements regarding self-supporting overhang angles. However, this does not necessarily mean that no support material is needed. Even when parts have no surfaces violating the critical overhang angle, there might be other reasons related to the AM process to add support structures: to increase local heat conduction to prevent overheating, to limit part distortions, or to provide sufficient support for follow-up machining operations. These aspects have not been taken into account in the present AM filter, which purely targets the overhang angle criterion. Still, even when for other reasons certain additional supports are necessary, saving costs by eliminating the overhang-related support structures still offers a benefit.

The examples also illustrate, that while for certain orientations performance of designs may reduce by the imposed AM restrictions, most cases performed comparable to reference designs optimized without AM filter. In several cases, the designs obtained with AM restrictions even outperformed the refer-

ence design. In general, adding more restrictions to an optimization problem cannot improve its global optimum. However, in the high-dimensional nonconvex optimization problems solved in topology optimization using gradient-based methods, finding the global optimum is unlikely in practice. In all three example problems considered in Section 4, it was established that the reference designs were local optima, and superior alternative optima were found for designs obtained in certain printing directions. It cannot be inferred that use of the AM filter will result in superior designs, but clearly it is not *a priori* certain that adding AM restrictions will significantly reduce performance.

While the examples show how the proposed AM filter can be applied successfully, its limitations should also be noted. Firstly, the filter is defined on a regular grid, and only build orientations in principal directions can be considered. Through a mapping procedure it can presumably be extended to unstructured meshes and arbitrary orientations, but this is yet to be developed. Secondly, on a mesh with cube-shaped elements, the critical overhang angle is fixed to 45°. Although this is a commonly used angle, when needed it is easily modified by changing the aspect ratio of the elements. Thirdly, while it was not observed in the examples, enclosed holes may appear in the optimized designs, where powder would be trapped during the printing process. The AM filter does not prevent the formation of such holes. Possibly the approach recently proposed by Liu *et al.* [28] can be combined with this filter to solve this problem.

Finally, a general limitation of the presented approach is that only a single build direction is considered, which cannot be altered during the optimization process. This places the responsibility on the designer to choose the most suitable orientation. While in practice there can be various reasons to prefer a certain orientation (tolerances, surface finish, build height, etc.), it would be of interest to also optimize the build direction simultaneously with the part geometry.

6. Concluding remarks

This paper presents a method to generate fully self-supporting, optimized part geometries in three dimensions. It combines established density-based topology optimization with a simplified AM process model, implemented as a layerwise nonlinear spatial filter defined on a uniform structured mesh. This formulation is able to rigorously exclude geometries from the design space that violate the overhang angle criteria typically encountered in AM processes. As a result, optimized designs do not require additional sacrificial structures to support overhangs, which simplifies post-processing and reduces cost.

The method has been applied to typical 3D topology optimization test problems, and proved able to generate designs that suitably respected the specified critical overhang angle, for a specified build direction. The computational cost of the additional AM filter operations proved negligible compared to the part analysis performed in each iteration. Also, it was observed that the use of the proposed AM restriction does not necessarily result in reduced performance. On the contrary, in all cases part orientations could be identified, for which the AM-restrained design outperformed the design found through conventional unrestricted topology optimization.

This new method is expected to contribute to simplification of the use of TO for AM, by removing complications related to overhang-based geometrical restrictions. The numerical examples have shown, that the chosen build orientation can have a significant impact on the achievable performance, depending on the particular case. Presently this is still an aspect that must be chosen *a priori* separately from the optimization process, and based on the results of the test cases it is recommended to always explore different orientations. A next challenge is to also include build orientation in the optimization problem. As a further future direction more process-specific refinement of the applied AM process model is expected, to include other criteria besides overhang angles, *e.g.* part distortion, residual stresses and overheating.

7. Acknowledgement

The author would like to thank Krister Svanberg for providing the Fortran implementation of his Method of Moving Asymptotes, which was used in this work.

Appendix: Sensitivity analysis

Here a condensed description of the adjoint sensitivity analysis of a response f with respect to blueprint density field $\mathbf{b}$ is given. Responses are computed on the basis of the printed density field $\mathbf{p}$, where each layer $\mathbf{p}_k$ depends on blueprint layer $\mathbf{b}_k$ and underlying printed layer $\mathbf{p}_{k-1}$. With Eq. 1, this relation is denoted by:

$$\mathbf{p}_k = \mathrm{smin}(\mathbf{b}_k, \mathbf{p}_{k-1}), \quad k = 2 \dots n_z.$$

Sensitivities $\partial f / \partial \mathbf{p}$ are computed via adjoint sensitivity analysis as discussed in Section 3. Next, we define the augumented response $\tilde{f}$ as:

$$\tilde{f} = f(\mathbf{p}(\mathbf{b})) + \sum_{k=2}^{n_z} \boldsymbol{\lambda}_k^T \left(\mathrm{smin}(\mathbf{b}_k, \mathbf{p}_{k-1}) - \mathbf{p}_k \right), \tag{14}$$

with multiplier vectors $\boldsymbol{\lambda}_k$. For the first layer, since $\mathbf{p}_1 \equiv \mathbf{b}_1$, we find $\partial f / \partial \mathbf{b}_1 = \partial f / \partial \mathbf{p}_1$. For subsequent layers, differentiation of Eq. 14 gives:

$$\frac{\partial \tilde{f}}{\partial \mathbf{b}_m} = \sum_{k=2}^{n_z} \left\{ \frac{\partial f}{\partial \mathbf{p}_k} \frac{\partial \mathbf{p}_k}{\partial \mathbf{b}_m} + \boldsymbol{\lambda}_k^T \left(\frac{\partial \mathrm{smin}}{\partial \mathbf{b}_m} \delta_{km} + \frac{\partial \mathrm{smin}}{\partial \mathbf{p}_{k-1}} \frac{\partial \mathbf{p}_{k-1}}{\partial \mathbf{b}_m} - \frac{\partial \mathbf{p}_k}{\partial \mathbf{b}_m} \right) \right\} \tag{15}$$

where δ_{km} denotes the Kronecker delta, and $1 < m \leq n_z$. Since printed densities only depend on blueprint densities in underlying layers, terms in the summations with $k < m$ vanish. This allows Eq. 15 to be rewritten as:

$$\frac{\partial \tilde{f}}{\partial \mathbf{b}_m} = \frac{\partial f}{\partial \mathbf{p}_m} \frac{\partial \mathbf{p}_m}{\partial \mathbf{b}_m} + \sum_{k=m+1}^{n_z} \left\{ \left(\frac{\partial f}{\partial \mathbf{p}_k} - \boldsymbol{\lambda}_k^T \right) \frac{\partial \mathbf{p}_k}{\partial \mathbf{b}_m} + \boldsymbol{\lambda}_k^T \frac{\partial \mathrm{smin}}{\partial \mathbf{p}_{k-1}} \frac{\partial \mathbf{p}_{k-1}}{\partial \mathbf{b}_m} \right\}$$

where $\partial \mathbf{p}_m / \partial \mathbf{b}_m = \partial \mathrm{smin} / \partial \mathbf{b}_m$ was used. From here, by rearranging the terms in the summation and reindexing, it can be found that:

$$\begin{aligned} \frac{\partial \tilde{f}}{\partial \mathbf{b}_m} = &\left(\frac{\partial f}{\partial \mathbf{p}_m} + \boldsymbol{\lambda}_{m+1}^T \frac{\partial \mathrm{smin}}{\partial \mathbf{p}_m} \right) \frac{\partial \mathrm{smin}}{\partial \mathbf{b}_m} + \left(\frac{\partial f}{\partial \mathbf{p}_{n_z}} - \boldsymbol{\lambda}_{n_z}^T \right) \frac{\partial \mathbf{p}_{n_z}}{\partial \mathbf{b}_m} \\ &+ \sum_{k=m+1}^{n_z - 1} \left(\frac{\partial f}{\partial \mathbf{p}_k} - \boldsymbol{\lambda}_k^T + \boldsymbol{\lambda}_{k+1}^T \frac{\partial \mathrm{smin}}{\partial \mathbf{p}_k} \right) \frac{\partial \mathbf{p}_k}{\partial \mathbf{b}_m}. \end{aligned}$$

This equation holds for $1 < m \leq n_z$. Computing $\partial \mathbf{p}_k / \partial \mathbf{b}_m$-terms can be avoided when choosing the multipliers as:

$$\boldsymbol{\lambda}_k^T = \frac{\partial f}{\partial \mathbf{p}_k} + \boldsymbol{\lambda}_{k+1}^T \frac{\partial \text{smin}}{\partial \mathbf{p}_k} \qquad \text{for } 1 < k < n_z,$$

and $\boldsymbol{\lambda}_{n_z}^T = \partial f / \partial \mathbf{p}_{n_z}$. With this, computing consistent sensitivities $\partial f / \partial \mathbf{b}$ reduces to the procedure described in Section 2.2.

References

[1] I. Gibson, D. Rosen, B. Stucker, Additive Manufacturing Technologies, Springer, 2015.

[2] D. Espalin, D. Muse, E. MacDonald, R. Wicker, 3D printing multifunctionality: structures with electronics, The International Journal of Advanced Manufacturing Technology 72 (5-8) (2014) 963–978.

[3] W. Gao, Y. Zhang, D. Ramanujan, K. Ramani, Y. Chen, C. Williams, C. Wang, Y. Shin, S. Zhang, P. Zavattieri, The status, challenges, and future of additive manufacturing in engineering, Computer-Aided Design 69 (2015) 65–89.

[4] E. Atzeni, A. Salmi, Economics of additive manufacturing for end-usable metal parts, The International Journal of Advanced Manufacturing Technology 62 (9-12) (2012) 1147–1155.

[5] C. Emmelmann, J. Kranz, D. Herzog, E. Wycisk, Laser additive manufacturing of metals, in: Laser Technology in Biomimetics, Springer, 2013, pp. 143–162.

[6] M. Bendsøe, N. Kikuchi, Generating optimal topologies in structural design using a homogenization method, Computer methods in applied mechanics and engineering 71 (2) (1988) 197–224.

[7] M. Cavazzuti, A. Baldini, E. Bertocchi, D. Costi, E. Torricelli, P. Moruzzi, High performance automotive chassis design: a topology optimization based approach, Structural and Multidisciplinary Optimization 44 (1) (2011) 45–56.

[8] J.-H. Zhu, W.-H. Zhang, L. Xia, Topology optimization in aircraft and aerospace structures design, Archives of Computational Methods in Engineering (2015) 1–28.

[9] O. Sigmund, K. Maute, Topology optimization approaches, Structural and Multidisciplinary Optimization 48 (6) (2013) 1031–1055.

[10] J. Deaton, R. Grandhi, A survey of structural and multidisciplinary continuum topology optimization: post 2000, Structural and Multidisciplinary Optimization 49 (1) (2014) 1–38.

[11] D. Rosen, Design for additive manufacturing: Past, present, and future directions, Journal of Mechanical Design 136 (9) (2014) 090301.

[12] D. Wang, Y. Yang, Z. Yi, X. Su, Research on the fabricating quality optimization of the overhanging surface in slm process, The International Journal of Advanced Manufacturing Technology 65 (9-12) (2013) 1471–1484.

[13] R. Mertens, S. Clijsters, K. Kempen, J.-P. Kruth, Optimization of scan strategies in selective laser melting of aluminum parts with downfacing areas, Journal of Manufacturing Science and Engineering 136 (6) (2014) 061012.

[14] J. Kranz, D. Herzog, C. Emmelmann, Design guidelines for laser additive manufacturing of lightweight structures in TiAl6V4, Journal of Laser Applications 27 (S1) (2015) S14001.

[15] G. Strano, L. Hao, R. Everson, K. Evans, A new approach to the design and optimisation of support structures in additive manufacturing, The International Journal of Advanced Manufacturing Technology 66 (9-12) (2013) 1247–1254.

[16] J. Vanek, J. Galicia, B. Benes, Clever support: efficient support structure generation for digital fabrication, in: Computer Graphics Forum, Vol. 33, Wiley Online Library, 2014, pp. 117–125.

[17] F. Calignano, Design optimization of supports for overhanging structures in aluminum and titanium alloys by selective laser melting, Materials & Design 64 (2014) 203–213.

[18] A. Hussein, L. Hao, C. Yan, R. Everson, P. Young, Advanced lattice support structures for metal additive manufacturing, Journal of Materials Processing Technology 213 (7) (2013) 1019–1026.

[19] D. Brackett, I. Ashcroft, R. Hague, Topology optimization for additive manufacturing, in: Proceedings of the Solid Freeform Fabrication Symposium, Austin, TX, 2011, pp. 348–362.

[20] M. Leary, L. Merli, F. Torti, M. Mazur, M. Brandt, Optimal topology for additive manufacture: A method for enabling additive manufacture of support-free optimal structures, Materials & Design 63 (2014) 678–690.

[21] A. Gaynor, J. Guest, Topology optimization for additive manufacturing: considering maximum overhang constraint, in: 15th AIAA/ISSMO multidisciplinary analysis and optimization conference, 2014, pp. 16–20.

[22] M. Langelaar, An additive manufacturing filter for topology optimization of print-ready designs, structural and Multidisciplinary Optimization, in review (2016, forthcoming).

[23] M. Bendsøe, Optimal shape design as a material distribution problem, Structural optimization 1 (4) (1989) 193–202.

[24] T. Bruns, D. Tortorelli, Topology optimization of non-linear elastic structures and compliant mechanisms, Computer Methods in Applied Mechanics and Engineering 190 (26) (2001) 3443–3459.

[25] M. Bendsøe, O. Sigmund, Topology Optimization - Theory, Methods and Applications, Springer-Verlag, Berlin, 2003.

[26] K. Svanberg, The method of moving asymptotes - a new method for structural optimization, International Journal for Numerical Methods in Engineering 24 (2) (1987) 359–373.

[27] G. Rozvany, A critical review of established methods of structural topology optimization, Structural and Multidisciplinary Optimization 37 (3) (2009) 217–237.

[28] S. Liu, Q. Li, W. Chen, L. Tong, G. Cheng, An identification method for enclosed voids restriction in manufacturability design for additive manufacturing structures, Frontiers of Mechanical Engineering 10 (2) (2015) 126–137.